International Journal of Heat and Mass Transfer 150 (2020) 119325

Contents lists available at ScienceDirect

International Journal of Heat and Mass Transfer

journal homepage: www.elsevier.com/locate/hmt

Analysis of the enhancing mechanism in pool boiling heat transfer through wetting speed for rough aluminum surfaces with FC-72

Jun Kim, Jeongwoo Yeom, Daeyoung Kong, Hyoungsoon Lee*, Seok-min Kim*

Department of Mechanical Engineering, Chung-Ang University, Seoul, 06974, Republic of Korea

ARTICLE INFO

Article history:
Received 10 June 2019
Revised 30 December 2019
Accepted 6 January 2020
Available online 18 January 2020

Keywords:
Critical heat flux
Pool boiling
Wetting speed
Random rough surface
Unidirectional rough surface
Fluorocarbon liquid

ABSTRACT

This study focused on the critical heat flux (CHF) characteristics in pool boiling heat transfer for various rough surfaces with FC-72. In particular, the enhancing effect of the CHF according to the direction of roughness was verified. Random rough surfaces with various roughness range were fabricated by the polishing process, and a unidirectional rough surface (URS) with hairlines on the surface was prepared for comparison. We proposed a CHF prediction model to analyze the enhancement of CHF on rough surfaces. The proportional relationship between the increase in CHF and the difference between the areal wetting speed on a rough surface and on a smooth surface was verified. The experimental CHF data were located in the median range of the proposed model, which was defined using the range of the Taylor instability wavelength in the Zuber model. In addition, the proposed model can predict the CHF for URS sample using the average of the areal wetting speed in both parallel and normal directions.

1. Introduction

The demand for high-efficiency thermal management systems in various fields such as heat exchangers and cooling of integrated circuits has increased remarkably owing to rapid industrial development. Boiling heat transfer has been regarded as the most practical solution to achieve such high efficiency [1–3], with much higher heat flux than the conventional heat transfer [4].

The critical heat flux (CHF) is the most important parameter that describes the thermal limit during boiling heat transfer [5]. To ensure stable utilization of the heat transfer system, the CHF must be identified or predicted beforehand to prevent the wall superheat from entering the film boiling region [6]. Continual increases in heat flux over the CHF results in the heated surface being entirely covered by the vapor layer, which is known as film boiling [4]. Once the heated surface enters the film boiling regime, heat transfer by boiling sharply decreases and the corresponding surface temperature rapidly increases, which damages the system [7]. Various theoretical prediction models have been proposed to predict the CHF. Some studies have focused on using the contact angle (CA) as an essential parameter for CHF prediction [8–11]. CA-based prediction models can predict the CHF accurately when polar liquids such as water and acetone are used, owing to the high surface energy of such liquids; that is, the CA is relatively easy to measure. However, non-polar liquids such as hydrocarbon and fluorocarbon liquid are highly wetting fluids owing to their low surface energy; thus, performing CA measurement is rather difficult, if not impossible [12,13]. A CHF prediction method based on parameters that are independent of CA is therefore needed for a broad theoretical analysis of boiling heat transfer. Recently, some studies have found a strong relationship between wetting characteristics and CHF; however, previous studies cannot be adopted for various rough surfaces as they depend on geometrical parameters of engineered surfaces [12,14,15].

Recent advances in micro/nanofabrication technology have enabled the fabrication of engineered microstructures, which has enhanced the CHF [16–20]. Table 1 lists the experimental studies for pool boiling heat transfer on rough surfaces with FC-72. The results from random roughness showed 12% to 32% enhancement in CHF [21,22], whereas the engineered surface showed 50% to 190% enhancement in CHF compared with the smooth surface [12,23,24]. Despite enhancement in the CHF, microstructures are rarely adopted in industry due to two main reasons: the processing cost and material scarcity. From this perspective, surface roughening techniques using low-cost processes such as grinding, polishing, and corrosion are considered practical alternatives for engineered microstructures in order to enhance the CHF [25]. Results from surface roughening techniques show only 30–40% enhancement or the upper limitation of the CHF [26–30]. Although the potential CHF enhancement obtained by using these techniques is limited, their low processing cost makes them suitable for mass production. Besides, these methods can be employed in

* Corresponding authors.
E-mail addresses: leeh@cau.ac.kr (H. Lee), smkim@cau.ac.kr (S.-m. Kim).

https://doi.org/10.1016/j.ijheatmasstransfer.2020.119325
0017-9310/

Table 1
Experimental studies for pool boiling heat transfer on rough surfaces with FC-72.

Author	Surface material	Roughness range	Enhancement in CHF
Golobič and Ferjančič [21]	Steel 1010 (Ribbon heater)	$0.07 \le R_a \le 1.5$ μm (Polishing with sandpaper)	12% ($R_a = 1.5$ μm)
Ferjančič and Golobič [22]	Stainless steel 302 (Ribbon heater)	$0.02 \le R_a \le 1.5$ μm (Polishing with sandpaper)	31.7% ($R_a = 1.5$ μm)
Honda et al. [23]	Silicon	$r = 2.2$ and $r = 2.2$ with submicron roughness	80% ($r = 2.2$), 130% ($r = 2.2$, roughened)
Wei and Honda [24]	Silicon	$1.0 \le r \le 7.67$	190% ($r = 6.4$)
Nguyen et al. [12]	Silicon	$1.0 \le r \le 3.2$	50% ($r = 3.2$)

various types of heat exchangers since they can be easily applied to different types of metal substrates [28].

Commercially available metal plates, which are fabricated by rolling or extrusion processes, usually have hairlines on their surfaces showing unidirectional roughness. In this case, CHF enhancement would be achieved with no additional surface roughness control processes. Thus, the boiling heat transfer characteristics must be evaluated by comparing commercial metal plates with unidirectional roughness and that with random roughness through surface roughening techniques.

In this study, we experimentally compared the CHF characteristics of random roughness using polishing process and an industrially rolled aluminum surface with unidirectional roughness. The experimental results were also applied to CA-based CHF prediction models to analyze the difference in the CHF characteristics for unidirectional roughness and various random roughness. The limitation of the existing CA-based prediction model was addressed using a fluorocarbon liquid (FC-72) which is widely used as a heat transfer fluid. Finally, we proposed a new CHF prediction model based on the wetting characteristics for liquids with high wettability, and the prediction results were compared with experimental data.

2. Sample preparation and surface characteristics

2.1. Preparation of rough surfaces

A total of six types of aluminum test samples with different random roughness were fabricated using commercial pure aluminum plates (AA1050; size of 30 mm × 30 mm^2 and thickness of 1 mm). The polishing process was performed for 60 s to 180 s using a mechanical polisher (LavoPol-5, Struers, Denmark) with a rotation speed of 300 RPM. P600 to P2000 graded sandpapers (KA161 and CC261, Deerfos, Republic of Korea) were used to produce various random roughness surfaces. We also fabricated a smooth surface using a polishing process with alumina compound, which was used as the reference. The test samples were labeled A to F in order of increasing surface roughness.

Fig. 1(a)–1(f) show the 3D-profiles of random rough surfaces obtained using 3D confocal microscope (OLS4100-SWF, Olympus Co., Ltd., Japan). As shown in Fig. 1(a) and 1(b), samples A and B have a relatively uniform and smooth surface profile. However, samples C–F formed irregular rough structures on the surface, as shown in Fig. 1(c)–1(f). Fig. 1(g) shows a 3D-profile of unidirectional rough surfaces (URS) obtained from an industrially rolled aluminum plate. Clear hairlines are observed on the surface of the plates in the direction of the rolling process. The direction parallel to the hairlines is designated as the parallel direction and that perpendicular to the hairlines is designated as the normal direction.

Table 2 lists the measured roughness parameters of the test samples and its standard deviations, namely the root mean square (RMS) roughness R_q and roughness factor r. The values of R_q for each direction and r were determined by averaging the measured data from four measurement points obtained using a 3D confocal microscope. R_q is the standard deviation of the measured surface height profile, which is calculated using the following equation:

$$R_q = \left(\frac{\sum (z_i - z_m)^2}{N} \right)^{1/2} \tag{1}$$

where z_i is the measured height at each point, z_m is the measured average height of the surface, and N is the number of sampling points. The random rough surfaces have uniform R_q regardless of its direction, whereas there is a significant difference in the R_q of the URS sample according to the direction parallel to or normal to the hairlines on the surface. r is defined as the ratio of the surface area of the rough surface A_R to the projection area A_P of the measurement area, as given below:

$$r = \frac{A_R}{A_P} \tag{2}$$

r tends to increase with increasing surface roughness. In the case of the URS sample, however, the value of r is significantly smaller than that of sample C, which has a similar mean value of R_q as the URS sample.

2.2. Measurement of contact angle

Fig. 2(a) depicts the measurement setup for the static CA of each test sample. The measurements were repeated three times for each direction of the test sample fabricated for the pool boiling experiment. The test environment was maintained at 24 ± 1 °C, and the test sample was placed inside a sealed chamber to minimize measurement error due to evaporation of FC-72. The sealed chamber has a volume of 0.86 L and was filled with 0.25 L of FC-72, and a cloth bundle made of porous fiber was immersed in the FC-72 to promote evaporation of the fluid.

Measurements were conducted after a waiting period of 20 min to achieve a fully saturated environment in the chamber. A constant volume of pendant droplet was maintained during the measurement using a micropipette (P-2, Gilson Inc., USA). Although a small volume of droplet can enhance the accuracy of CA measurement [31], it is extremely difficult to measure the CA because the droplet easily spreads on the surface and evaporates [32]. Thus, we applied the traditional tangent method for CA measurement, which ensures independence between the volume of a sessile droplet and the CA [33]. Finally, 1.0 μL of droplet volume was experimentally determined as the appropriate volume for stable pendant droplets to form sessile droplets on the sample surfaces.

A high-speed camera (CR450×3, Optronis GmbH, Germany) was used to capture the shape of the sessile droplet at a frame rate of 120 FPS. The static CA of each test sample was measured using image analysis software (ImageJ), with an image captured 500 ms after the moment of fluid-surface contact. This time offset helps to maintain stable measurement conditions as it avoids the fluctuations of the sessile droplet, which occur during fluid-surface contact. Furthermore, the sessile droplet spreads on the surface within a few seconds in the super-hydrophilic cases; thus, the CA tends to converge to 0° due to the limitation of optical resolution [34]. As listed in Table 3, the measured result indicates that the static CA of fluorocarbon fluids with low surface tension was not remarkably

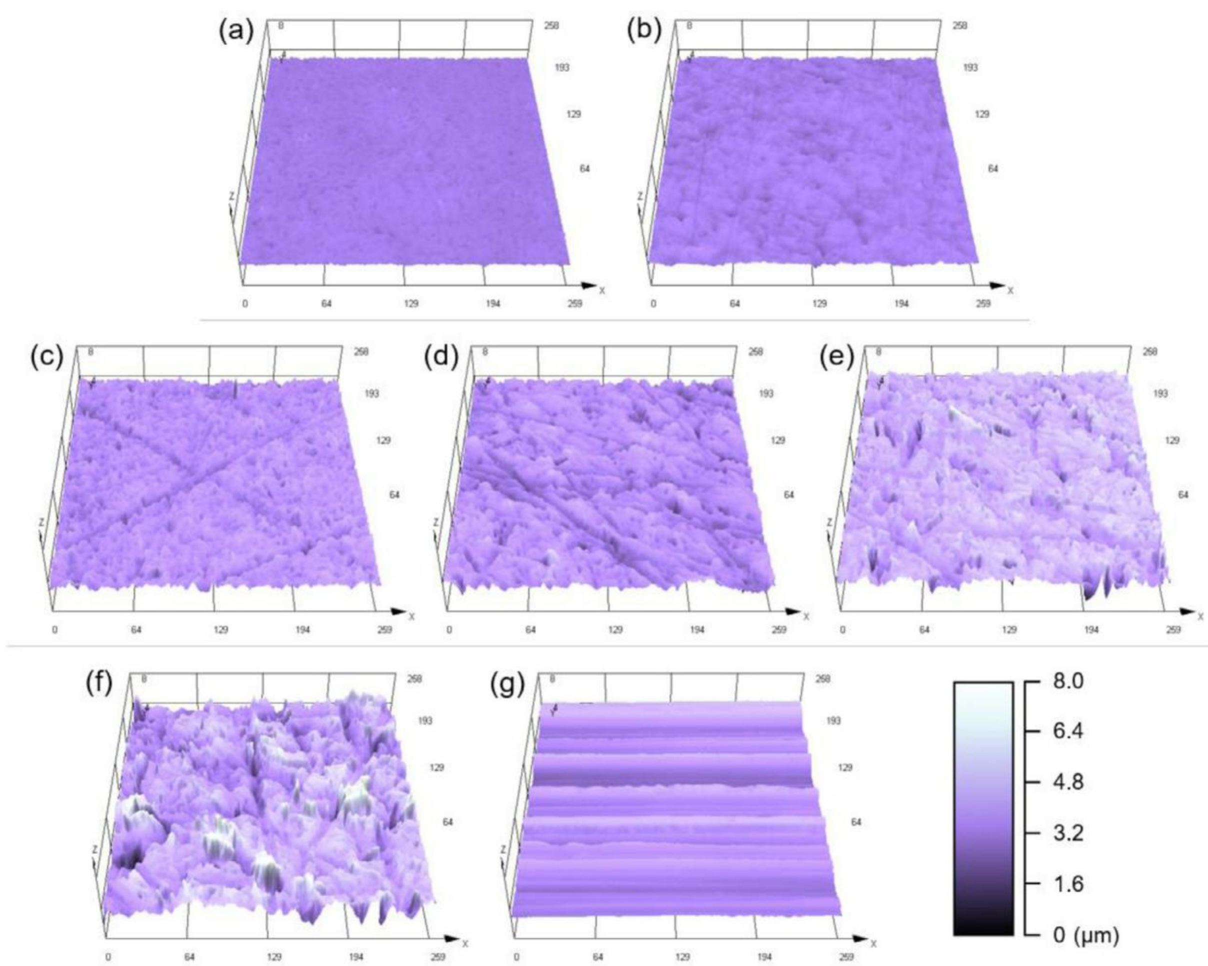

Fig. 1. 3D surface profiles of fabricated rough surfaces obtained using a 3D-confocal microscope with gray-scaled height range of 8 μm: (a) sample A with a smooth surface; (b–f) random rough surfaces arranged in the order of samples B to F; (g) URS sample.

Table 2
Processing condition and surface roughness data of the test samples (μm).

Sample	Processing condition	RMS roughness (R_q)			Roughness factor (r)
		Parallel	Normal	Mean	
A	Alumina Compound	0.09 ± 0.01	0.09 ± 0.01	0.09 ± 0.01	1.00 ± 0.00
B	P2000, 180s	0.16 ± 0.01	0.16 ± 0.03	0.16 ± 0.02	1.09 ± 0.01
C	P1200, 150s	0.28 ± 0.03	0.29 ± 0.04	0.28 ± 0.03	1.20 ± 0.03
D	P1000, 120s	0.37 ± 0.05	0.37 ± 0.05	0.37 ± 0.05	1.17 ± 0.03
E	P800, 90s	0.59 ± 0.06	0.54 ± 0.02	0.57 ± 0.05	1.24 ± 0.02
F	P600, 60s	0.86 ± 0.16	0.86 ± 0.07	0.86 ± 0.12	1.30 ± 0.01
URS	Rolling process	0.09 ± 0.01	0.43 ± 0.07	0.26 ± 0.17	1.05 ± 0.01

Table 3
Measured static CA of rough surfaces for parallel and normal direction (deg).

Type	A	B	C	D	E	F	URS
Contact angle (P)	15.61	12.61	12.96	14.48	13.59	13.65	10.85
Contact angle (N)	16.26	13.04	12.29	14.15	13.96	13.28	15.44
Mean	15.93	12.83	12.63	14.31	13.77	13.46	13.14

affected by the surface roughness. Furthermore, the random rough surfaces showed no significant difference in CA in the direction of the surface structure, whereas the URS sample showed approximately 5° difference in CA. Considering the pixel resolution, the uncertainty of CA measurement was estimated to be approximately ±5° (for details, see supplementary information S4.3).

2.3. Measurement of wetting distance

Fig. 2(b) illustrates the measurement setup for the wetting distance with respect to the surface roughness of each test sample. The sealed chamber was designed to take images from the top position, and a saturated environment should be maintained during

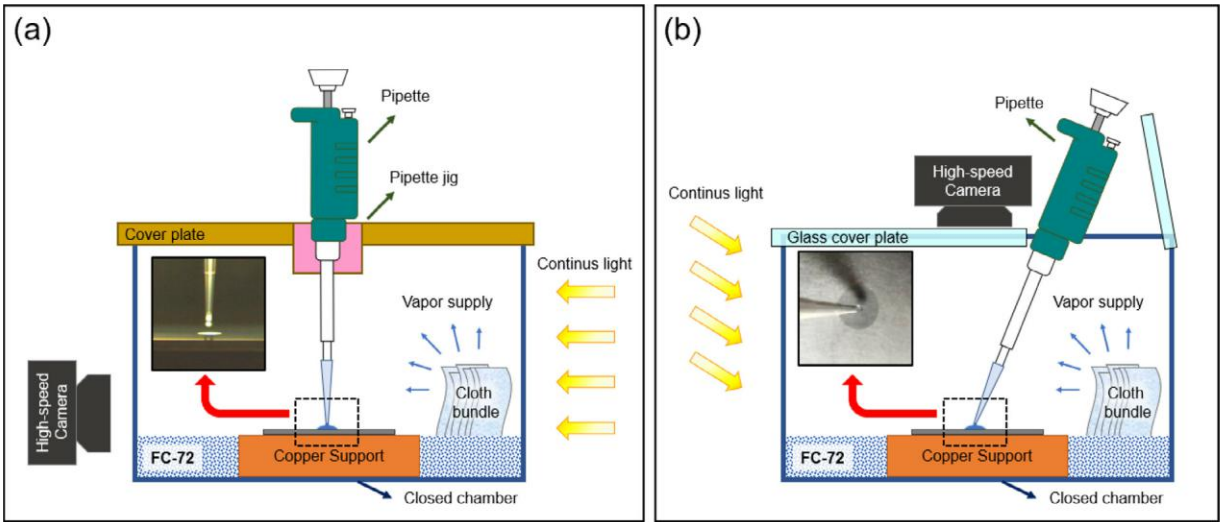

Fig. 2. Schematic of the measurement setup for: (a) static contact angle of rough surfaces; (b) wetting distance of rough surfaces.

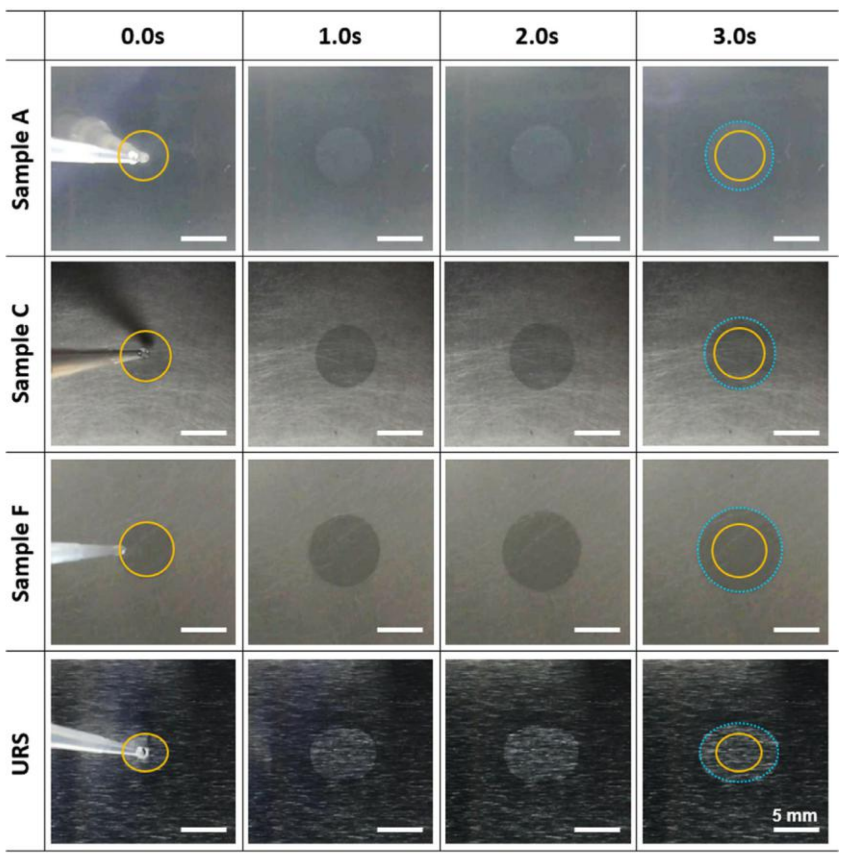

Fig. 3. Photographs of the wetting distance measurement. Circles are the wetting front at the initial state and after 3 s (dotted line).

the measurement. Therefore, the volume of the chamber is larger than CA measurement set up (1.65 L), and the upper portion of the chamber has a transparent B270 glass window to easily observe the surface wetting behavior. The copper block for mounting the test sample was precisely machined to 40 $\times$ 40 mm^2 and was then used as the reference length in the image analysis. The sealed chamber was filled with 0.4 L of FC-72 and a cloth bundle was immersed in the FC-72.

Each measurement was conducted after a waiting period of 20 min and repeated at least three times for each test sample and the test environment was maintained at 24 $\pm$ 1°C to minimize measurement error. A micropipette (P-2, Gilson Inc., USA) was used to precisely control the volume in the formation of a stable sessile droplet. In this measurement, a droplet volume of 2.0 μL was applied to supply sufficient liquid. A high-speed camera (CR450×3, Optronis GmbH, Germany) was used to record the wetting behavior at 120 FPS during the measurement. Fig. 3 shows the sequential snapshots of each specimen at 1 s intervals. The wetting area of sample A (smooth surface) increased at a relatively low rate, whereas that of sample F with high roughness increased at a rela-

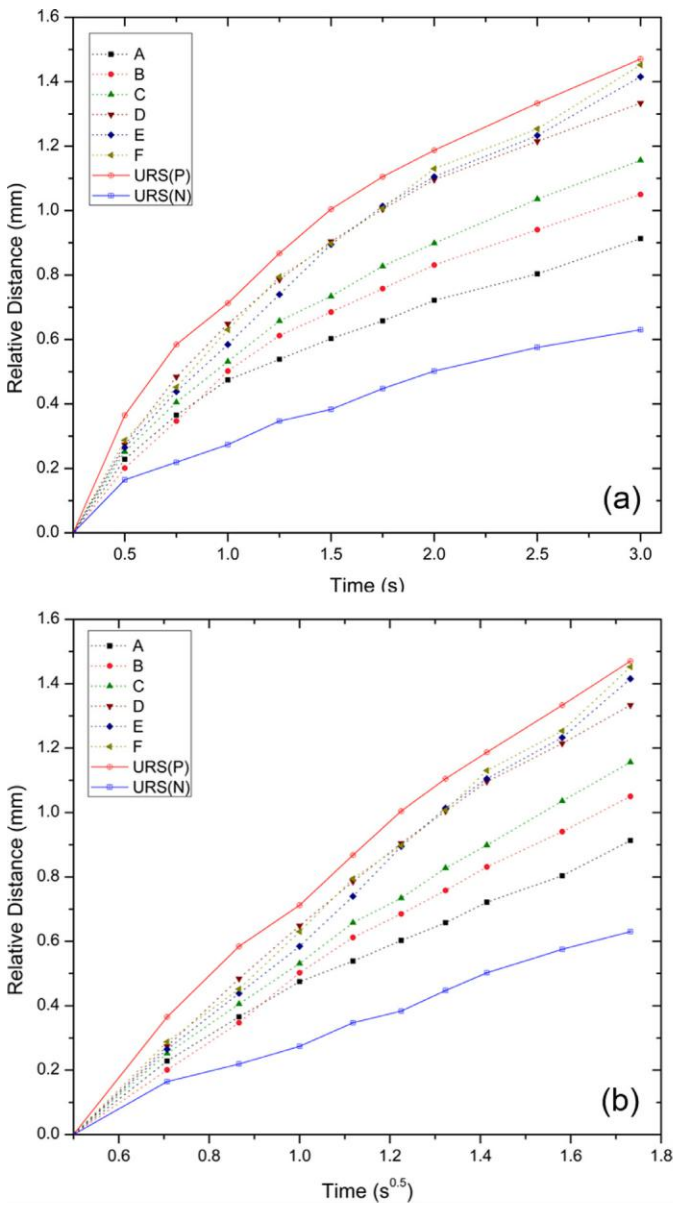

Fig. 4. Measured relative wetting distance of the test samples: (a) variation with time (s); (b) variation with the square root of time ($s^{0.5}$).

tively high rate. The wetting distance of each test sample were assessed quantitatively using image analysis software (ImageJ). Here, the diameter 500 ms after the moment of fluid-surface contact is defined as the initial reference diameter d_i to avoid fluctuations of the sessile droplet. For the uncertainty, the width of the pixel resolution was obtained as 54.8 ± 0.4 μm/pixel from calibration with the copper block measured as 730 ± 5 pixels. Thus, the distance uncertainty can be regarded as a pixel resolution, as ±0.055 mm. The relative wetting distance d_r was calculated by subtracting d_i from the wetting diameter d_w ($d_r = d_w$ - d_i). Using this method, errors due to variation in the initial wetting diameter were removed according to different wetting behaviors of each test sample.

Fig. 4(a) shows a comparison of the variation of the relative wetting distance d_r of each test sample with time (s). The measurements show that d_r increased along with the surface roughness, and the increase in d_r weakened over time. However, the increase in d_r due to surface roughness was saturated at surface roughness higher than $R_q = 0.37$ μm (sample D). For the URS sample, d_r in the parallel direction was similar to that of samples with high roughness, whereas a lower wetting distance than that of sample A was measured in the normal direction. This phenomenon is attributed to the fin effect, preventing or impeding fluid contact in the direction perpendicular to the surface pattern of the URS sample formed by a hairline [14].

Table 4
Calculated values of wicking coefficient using linear fitting of data from Fig. 4(b). Note that W is the slope of the linear fitted line.

Sample	W (mm/s$^{0.5}$)	R^2 for linear fitting	W^2 (mm^2/s)
A	0.704	0.980	0.495
B	0.855	0.991	0.731
C	0.924	0.994	0.853
D	1.091	0.986	1.190
E	1.155	0.996	1.334
F	1.165	0.996	1.358
URS (P)	1.166	0.984	1.360
URS (N)	0.502	0.992	0.252

The wetting distance can be described by the Washburn law [35] based on the balance of the capillary pressure and the viscous force [15,35,36]. Thus, the wetting distance x on a rough surface is proportional to the square root of time as given in the wetting correlation in Eq. 3 [36].

$$x(t) = \left(\frac{2}{3\beta} \frac{\cos\theta^* - \cos\theta_c}{\cos\theta_c} \frac{\sigma\delta}{\mu_f} t \right)^{1/2} \tag{3}$$

where β is an empirically determined factor related to the shape of the surface structure, whereas σ, δ, μ_f, and t are the surface tension of the fluid, the height of the pattern, the viscosity of the fluid, and time, respectively. Kim *et al.* [15] combined all the variables, except time, as the wicking coefficient W as given in Eq. 4, which was obtained experimentally:

$$x(t) = W \cdot t^{1/2} \tag{4}$$

Fig. 4(b) shows the variation of the measured relative wetting distance d_r with the square root of time. The slope of each test sample represents W. Table 4 summarizes the linear fitting results of each slope. In all cases, the coefficient of determination R^2 is 0.98 or higher, which indicates good agreement with the prediction obtained from the aforementioned Bico's wetting correlation [36]. As described in supplementary information S4.5, the maximum uncertainty for W was estimated as ±0.055 mm/s$^{0.5}$.

3. Pool boiling experiment

3.1. Pool boiling setup

Fig. 5 shows the pool boiling experimental setup. The boiling chamber is made of stainless steel 330 L with a square structure of 150 mm (length, width, and height). Four auxiliary heaters were installed in the chamber to maintain the fluid temperature at the boiling point. An air-cooled condenser was installed at the top of the boiling chamber to condense the vapor during boiling experiments. The test sample was attached to the top of the block using thermal grease (MX-4, ARCTIC, Switzerland; thermal conductivity = 8.5 W/m K). The space between the test sample and the chamber was sealed and insulated using a Teflon gasket (thermal conductivity = 0.25 W/m K). A copper heating block with two cartridge heaters (150 W for each heater) was installed at the bottom of the chamber to induce boiling on the surface of the test sample. The surrounding of the heating block was heavily insulated with silicone rubber, which has a low thermal conductivity (0.2 W/m K). Two thermocouples (AWG 24, J-Type, Omega Engineering Inc., USA) were inserted into the 10 mm-spaced drilled holes in the heat meter bar with a diameter of 1.5 mm and a depth of 15 mm. A multichannel thermo logger system

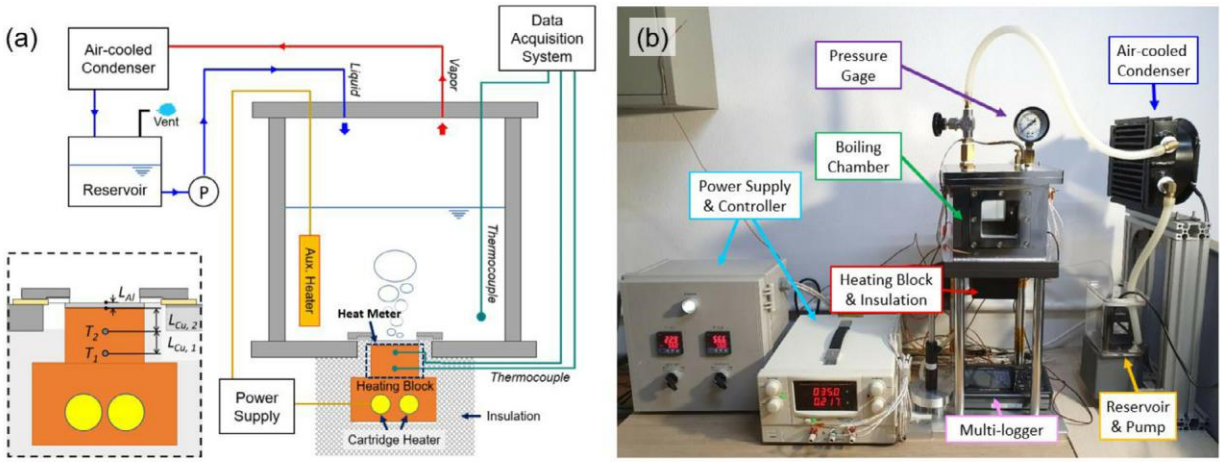

Fig. 5. Setup of the pool boiling experiment: (a) schematic view and flow diagram of the system. Detailed design for heating block was drawn inside the dashed line box; (b) photograph of the experimental facility.

(Graphtec GL220, DATAQ Instruments Inc., USA) was installed to record the temperature of each thermocouple at an interval of 2 s.

3.2. Experimental procedure and uncertainty

In this study, we used 1.6 L of FC-72 to immerse the auxiliary heater and the thermometer during the experiments. The boiling chamber was sealed with a lid to prevent inadvertent leakage of the vapor after pouring the working fluid. The auxiliary heaters were operated above the boiling point for 30 min for deaeration. We installed a vent valve and opened it during the experiment to remove gas and air inside. This deaeration process is very important for dielectric fluids since air can dissolve in FC-72 up to 48% by volume at room temperature and ambient pressure, which results in pseudo-enhancement of CHF similar to the subcooled case or increase in the uncertainty of the entire pool boiling experiment [37]. After deaeration, the control temperature of the heating block and auxiliary heaters were adjusted to the boiling point (56 °C at 1 atm) and was left for 1 h to reach thermal equilibrium state. The pool boiling experiments were conducted up to the film-boiling region where the surface temperature rises rapidly after the CHF. A proportional integral derivative (PID) controller controlled the temperature of the heating block. In the nucleate boiling regime, the temperature was controlled at a heating rate of 1 °C/min. After fully developed nucleate boiling, the temperature was controlled at a heating rate of 0.2 °C/min, whereas the auxiliary heaters were maintained at the boiling point. The evaporated working fluid was cooled through a condenser, and the volume of the working fluid was maintained constant using a circulation pump.

The heat flux q'' during the pool boiling experiment was estimated from the energy balance of the heat meter bar (neck of heating block) as follows:

$$Q_{in} = Q_{boil} + Q_{loss,lat} \tag{5}$$

where Q_{in} is the applied power, Q_{boil} is the amount of transferred heat due to natural convection and boiling on the test surface, and $Q_{loss,lat}$ is the lateral heat loss on the 4-side surfaces of the heat meter bar. Here, $Q_{loss,lat}$ was experimentally determined by comparing the applied electrical power and Q_{boil}. As a result, we found that $Q_{loss,lat}$ was less than 2.8% of the estimated amount of Q_{boil} near the CHF (for details, see supplementary information S1). Therefore, $Q_{loss,lat}$ can be regarded as low-biased uncertainty; hence, Eq. 5 can be expressed as $Q_{in} \sim Q_{boil}$. In this calculation, the difference in the area of the boiling surface A_{boil} (25 × 25 mm^2) and the cross-sectional area of the heat meter bar A_{in} (30 × 30 mm^2) was considered for estimating the heat flux on

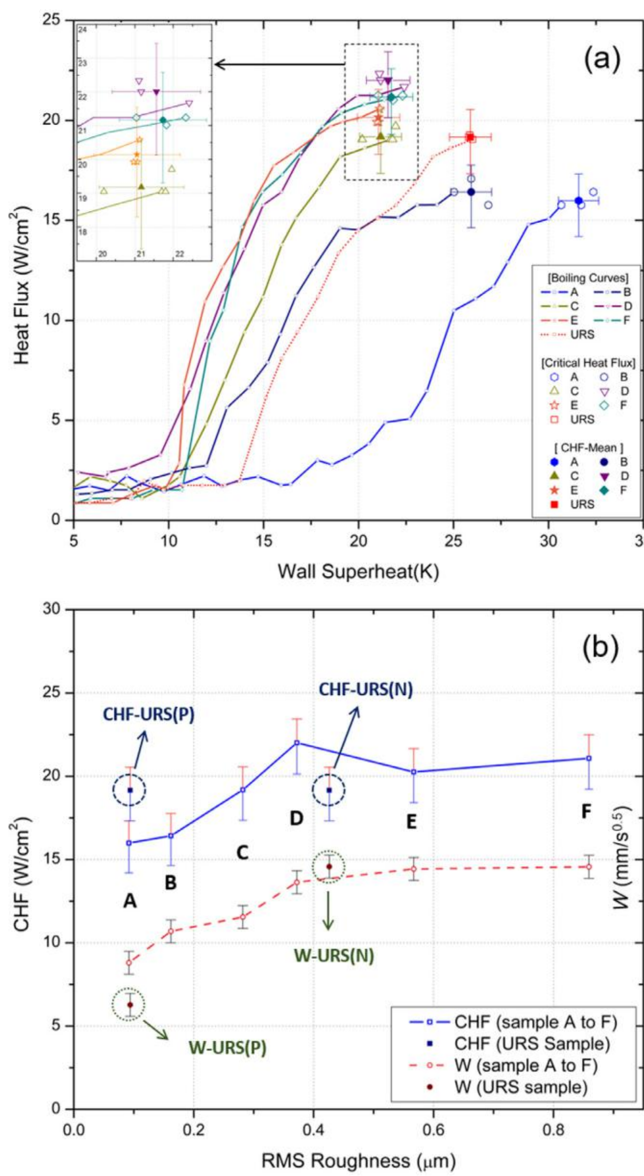

Fig. 6. Pool boiling results of rough surfaces: (a) boiling curves with critical heat flux values from repeated experiment; (b) a comparison of averaged critical heat flux and wicking coefficient with respect to the RMS roughness (R_q).

Table 5
Error sources and propagated uncertainty values in the pool boiling experiment.

Type	Uncertainty and error source	Error
Error source	Positioning error for the thermocouple hole	±0.02 mm
	Machining error for the thermocouple hole diameter	±0.05 mm
	Machining error for the dimension of heating block	±0.02 mm
	Reading error of J-type thermocouple	±0.15 K
	Thermal conductivity of Cu	±2.0 %
	Thermal conductivity of Al	±2.1 %
Propagated uncertainty	Thermal contact resistance	±13.59 %
	Critical heat flux	±6.49–8.37 %
	Surface temperature	±0.44–3.85 %

the test surface. Thus, Eq. 5 can be expressed as follows:

$$q''_{boil} = q''_{in} \times \frac{A_{in}}{A_{boil}} \tag{6}$$

where, q''_{boil} is the heat flux on the test surface (Q_{boil}/A_{boil}) and q''_{in} is the heat flux through the heat meter bar (Q_{in}/A_{in}). To estimate the heat flux on the sample surface, we applied Fourier's conduction law based on a one-dimensional heat transfer assumption as follows:

$$q''_{boil} = -k\frac{dT}{dz} \times \frac{A_{in}}{A_{boil}} = -k_{Cu}\frac{T_1 - T_2}{L_{Cu,1}} \times \frac{A_{in}}{A_{boil}} \tag{7}$$

T_1 and T_2 are temperatures from the lower and upper thermocouples installed in the heat meter bar. The temperature gradient dT/dz was estimated through the difference between T_1 and T_2. The distance dz was determined from the spacing between the two thermocouples, $L_{cu,1}$. To achieve the 1D heat transfer assumption, the offset distance $L_{cu,2}$ between the top of the heat meter bar and the measuring point for T_2 was experimentally determined as 10 mm. As described in Supplementary Information S2, the temperature gradient was linear above 8 mm of the offset distance.

The surface temperature of the test sample T_s can be calculated as described in the following equation using T_2, q''_{in}, thermal resistances, and dimensional difference between the boiling surface and the heat meter bar:

$$T_S = T_2 - q''_{in}\left(\frac{L_{Cu,2}}{k_{Cu}}\right) - q''_{in}\frac{A_{in}}{A_{boil}}\left(R''_{tc} + \frac{L_{Al}}{k_{Al}}\right) \tag{8}$$

The contact resistance R''_{tc} was calculated as 0.0957 cm^2 K/W using the procedure proposed by Cooke and Kandlikar [16] (for details, see Supplementary Information S3). The wall superheat ΔT_s was defined as T_s - T_{sat}, where T_{sat} is the boiling point of the working fluid.

The independent uncertainties in the pool boiling experiment were estimated and calculated through the second-power equation proposed by Kline and McClintock [38]. The positioning error of the drill hole for temperature measurement was ±0.02 mm, and the temperature reading error of the J-type thermocouple was ±0.15 K. In this experiment, the dimensions of the heat measurement parts, such as the heating block and the heat meter bar, were designed and machined with an accuracy of ±0.02 mm. For the test surfaces, the uncertainty of the thickness due to the polishing process was estimated from the measured data as ±0.1 mm. The uncertainty due to variation in the thermal conductivity according to the temperature variation of the material was confirmed to be ±2% for copper and ±2.1% for aluminum. The uncertainty of the CHF was estimated to be ±6.49–8.37%. In addition, the low-biased uncertainty due to the heat loss was estimated to be 2–2.8%. The

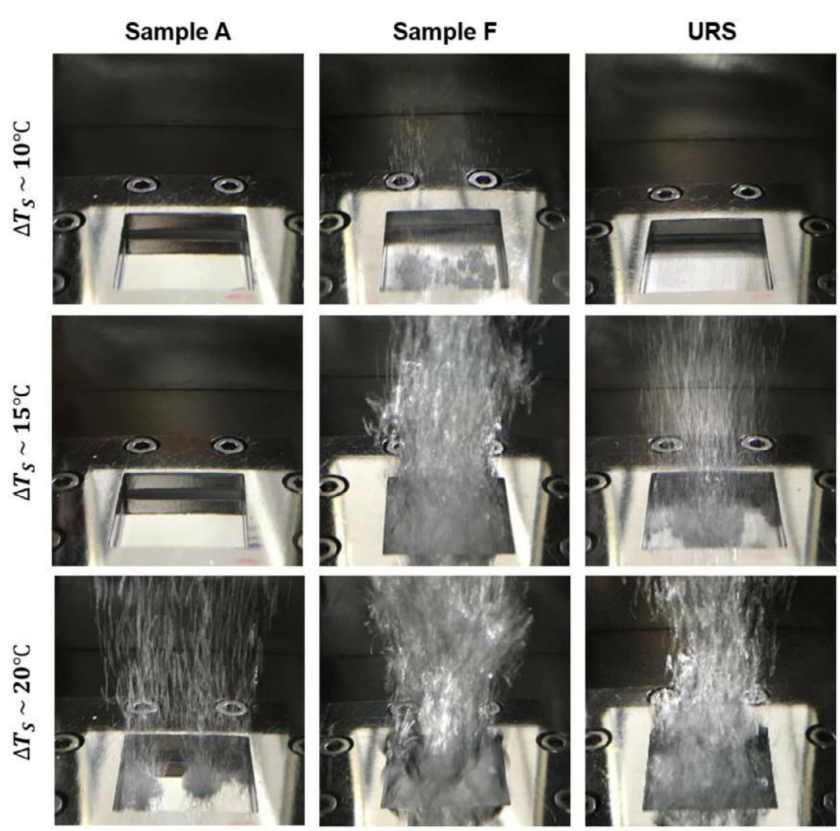

Fig. 7. Photographs of the pool boiling phenomenon for samples A and F, as well as URS sample. Each photograph was captured at the wall superheat temperatures of 10 °C, 15 °C, and 20 °C.

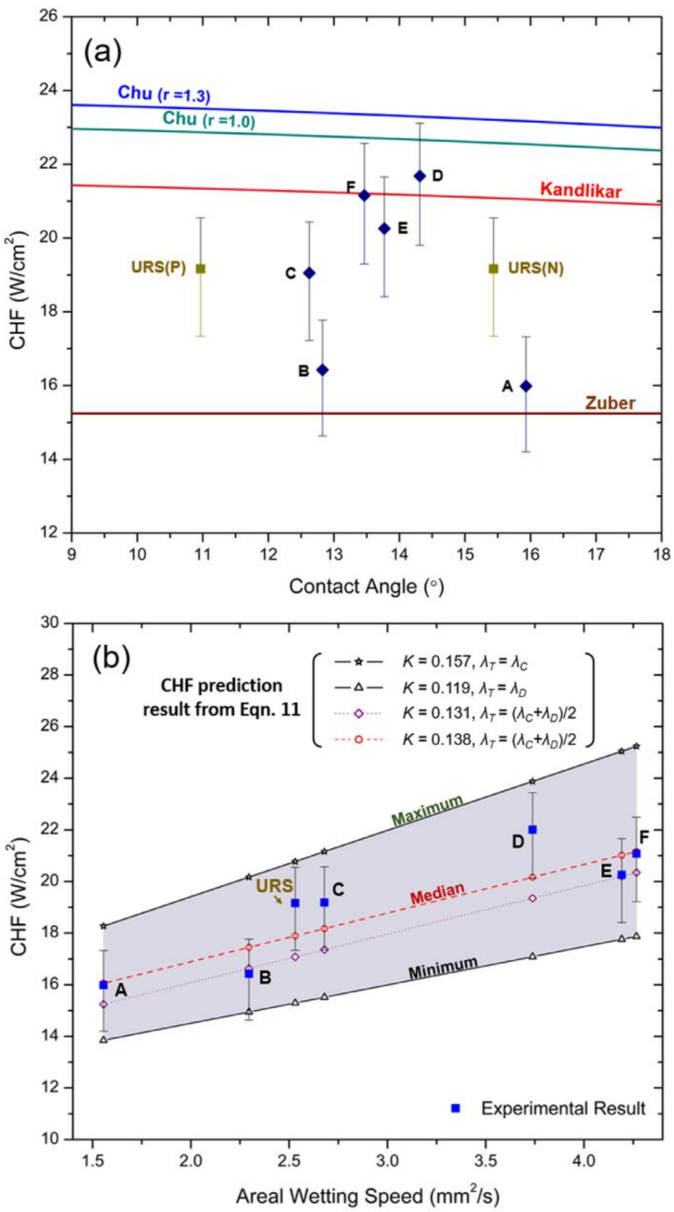

Fig. 8. (a) Comparison of the CHF values from the prediction models by Zuber [39], Kandlikar [10], and Chu *et al.* [11]. Experimental results are marked inside the dashed line box. (b) Variation of experimental CHF values of the rough surfaces with the line of the prediction model.

maximum error in the calculation of the contact resistance R''_{tc} was ±13.59%. Finally, the uncertainty of the estimated surface temperature was calculated as ±0.44–3.85%. The above results are summarized in Table 5 (for details, see Supplementary Information S4.1–4.3).

3.3. Pool boiling result

Fig. 6(a) shows the boiling curves measured for each test sample. For sample A (R_q = 0.09 μm), the incipience of nucleate boiling was observed at the wall superheat of ~ 20 °C. As the wall superheat increased, the heat flux increased, and the CHF was 15.99 ± 0.38 W/cm^2 at ~ 32 °C of the wall superheat. For sample B (R_q = 0.16 μm), the wall superheat at the incipience of nucleate boiling was ~ 12 °C. However, the measured CHF was 16.43 ± 0.93 W/cm^2, which is slightly higher than that of sample A. For samples C (R_q = 0.28 μm) and D (R_q = 0.37 μm), which have increased roughness than samples A and B, nucleate boiling started in the lower wall superheat. In these samples, the measured CHF values were 19.18 ± 0.29 W/cm^2 and 22.01 ± 0.47 W/cm^2, respectively. Samples E (R_q = 0.57 μm) and F (R_q = 0.86 μm), which have higher roughness, showed boiling curves similar to that of sample D. When the wall superheat was ~ 22 °C, the measured CHF values were 20.26 ± 0.47 W/cm^2 and 21.08 ± 0.21 W/cm^2, respectively. Considering the uncertainty of the calculated heat flux (~ 7 %), a significant change in the CHF with increase in surface roughness could not be confirmed. On the other hand, the URS sample exhibited similar CHF characteristics to sample C, whereas the overall boiling curve was located at a higher wall superheat. Fig. 7 shows the boiling phenomenon according to various wall superheats. The images clearly highlight the experimental results described above. In the case of sample F, bubbles were observed when the wall superheat was ~ 10 °C, whereas bubbles did not occur in sample A and URS sample. Furthermore, in sample F, it can be confirmed that boiling was activated at a low wall superheat compared to sample A and URS sample. Thus, surface roughening techniques not only enhance the CHF of URS or smooth surface but also significantly reduce the wall superheat required for boiling heat transfer.

The upper line in Fig. 6(b) shows a comparison of the measured CHF and the RMS roughness of each test sample. Similar to the boiling curve, the CHF tends to be enhanced at increasing surface roughness for samples A to D. However, there was no significant changes at higher roughness. A similar trend was also reported in previous studies [27,28,30]. In particular, the experimental CHF data reported by Ferjančič and Golobič [22] is similar to our experimental result. They studied the enhancement of CHF in FC-72 using rough stainless-steel plates with roughness in the range of 0.02 μm < R_a < 1.5 μm. Although the CHF was enhanced with increasing roughness, the change was not significant above a specific surface roughness (R_a > 0.3 μm). However, this result does not explain the relationship between the CHF and various types of surface roughness, including unidirectional roughness.

The dotted line in Fig. 6(b) indicates the *W*. It clearly shows that the CHF and *W* have a similar trend with respect to the RMS roughness. The *W* values of the URS sample in each direction show a clear directional dependency. Thus, it is particularly important to find the correlation between the CHF and wetting characteristics for accurate prediction of CHF characteristics on rough surfaces.

4. Analysis of enhancement of the CHF

First, the experimental results were compared with results obtained from some existing CHF prediction models. As shown in Fig. 8(a), the CHF predicted using Kandlikar's model [10] did not match the CHF results obtained from experiment. Kandlikar's model is based on CA with cosine terms, hence the predicted CHF increases when high wettability fluid is used. Chu *et al.* [11] considered the effect of surface roughness using Kandlikar's model. Although the predicted CHF tends to increase with increasing roughness factor, the CHF is did not match the prediction result from Chu's model (as listed in Table 2, the test samples have a roughness factor in the range of approximately 1.0 to 1.3). The main challenge of these models is that the surface roughness was not properly considered for predicting the CHF. Furthermore, the variation of the CAs is not significantly related to the surface roughness of the test sample, as shown in Fig. 8(a). Therefore, it is necessary to correlate the effect of surface roughness to CHF using parameters other than CA.

Analytical method based on the wetting characteristics is an alternative method for CHF prediction on rough surfaces [12,14,15]. Kim *et al.* [15] proposed the wickability–CHF model using Kandlikar's model as the reference CHF for a smooth surface. Recently,

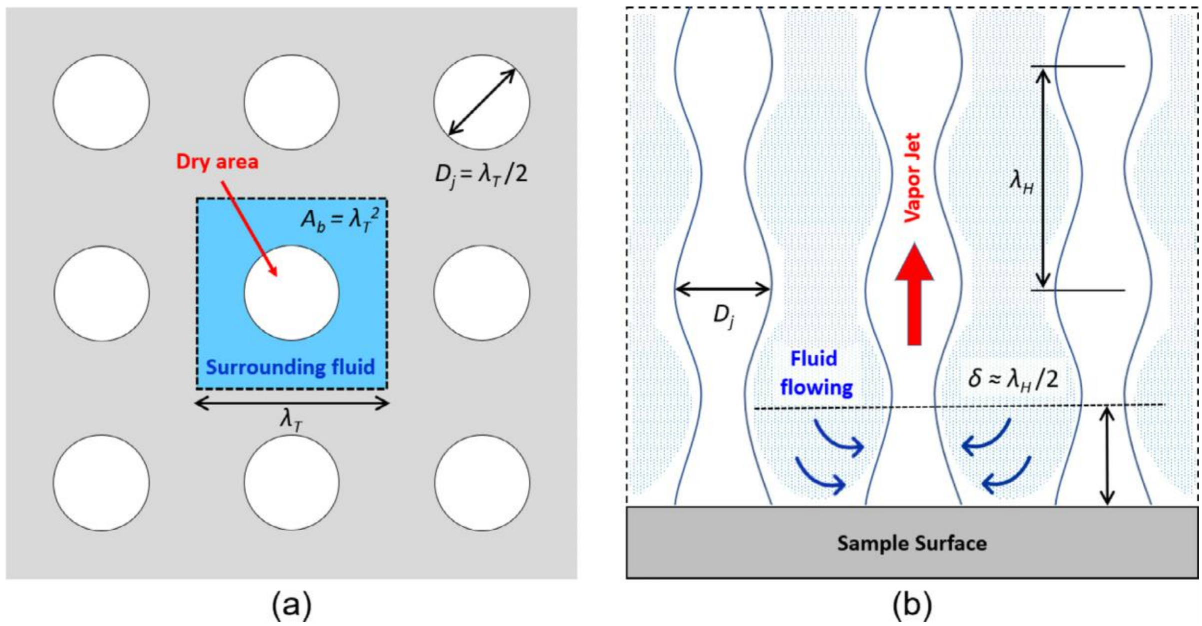

Fig. 9. Schematics of hydrodynamic instability when CHF occurs on a heated surface: (a) top view of the unit boiling area and dry area; (b) cross-sectional view of a vapor jet column.

Nguyen *et al.* [12] found a strong relationship between wetting speed and CHF using FC-72; Zuber's model was used as the reference CHF. Previous models cannot be adopted for random or unidirectional rough surfaces directly as they depend on geometrical parameters of engineered surfaces. However, the basic definition in these studies is reasonable owing to the strong relationship between CHF and wetting characteristics. Thus, we assumed that the CHF on a rough surface can be defined as follows:

$$q''_{CHF,\ rough} = q''_{smooth} + q''_{add}, \tag{9}$$

where q''_{smooth} is the reference CHF on an identically smooth surface and q''_{add} is the additional heat flux on a rough surface. For FC-72, it is reasonable to estimate q''_{smooth} by applying Zuber's model [39] since CHF is defined solely by the physical properties of the fluid. q''_{add} should be proportional to the additional amount of supplied liquid due to wicking on a rough surface. Thus, the additional heat flux can be calculated as follows:

$$q''_{add} = \frac{\Delta Q \rho_f h_{fg}}{A_b}, \tag{10}$$

where ΔQ is the additional volumetric flow rate (mm^3/s) supply due to surface conditions with respect to the smooth surface. ρ_f and h_{fg} are the fluid density and the latent heat at the boiling point of FC-72, respectively. As shown in Fig. 9(a), A_b is the unit boiling area, which can be described as the square of the Taylor instability wavelength as $A_b = \lambda_T{}^2$. According to the definition given in Zuber's model, λ_T is in the range from the critical wavelength λ_C to the most dangerous wavelength λ_D ($\lambda_C \le \lambda_T \le \lambda_D$). From this analysis, we can describe our CHF prediction model in the range of the maximum and minimum CHF, similar to Zuber's model.

In this study, ΔQ depends on the interfacial wetting dynamics on the heated surface. As depicted in the schematic in Fig. 10(a),

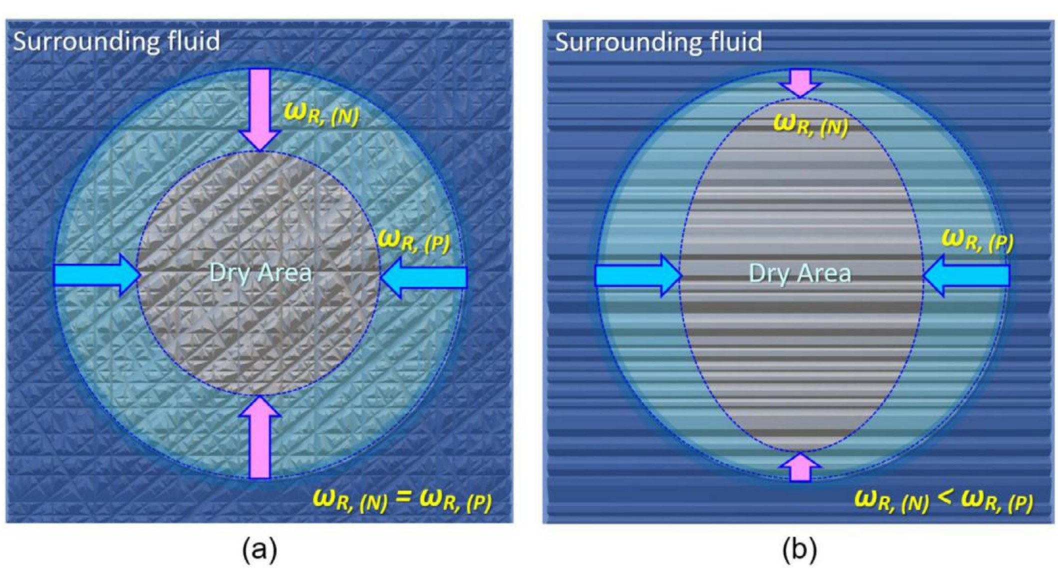

Fig. 10. Schematic of the wetting behavior on rough surfaces: (a) random rough surface; (b) unidirectional rough surface.

the wicking coefficient W is the radial change of the wetting area with the square root of time (mm/s$^{0.5}$). Since the surrounding fluid flows to the dry area in all circular directions, $\pi \bullet W^2$ (denoted as ω) is the areal wetting speed of the unit boiling area (mm^2/s). However, URS sample with unidirectional roughness exhibits two different wetting behaviors depending on its direction, as shown in Fig. 10(b). For this reason, the mean value of ω in each direction of the URS sample was used as an integrated value.

The areal wetting speed on rough surfaces ω_R can be assumed to be proportional to ΔQ with the thickness of the fluid supply layer δ as $\Delta Q \sim \delta \bullet \omega_R$. Although hydrostatic and hydrodynamic forces were considered in the reference CHF through Zuber's model, FC-72 has a nonzero wetting behavior even on smooth surfaces [12]. Therefore, the areal wetting speed of the smooth surface ω_S should be considered as part of the reference value. For this reason, ΔQ in Eq. 10 is described as $\delta(\omega_R\text{-}\omega_S)$ to include only the additional amount of the fluid on rough surfaces.

Fig. 9(b) depicts the cross-sectional view of the vertical vapor jet for heated surface. Haramura and Katto [40] proposed a correlation of δ with one-quarter of the Helmholtz instability wavelength (λ_H). They assumed δ to be a median value in the possible range from 0 to $\lambda_H/2$ because the exact value of δ was not defined at that time. Rajvanshi *et al.* [41] concluded that one-half of the Helmholtz instability wavelength (λ_H) gives a better correlation, which has been experimentally investigated by many researchers [42–44]. This can be written as $\pi \bullet \lambda_T/4$, where λ_H is $\pi \bullet \lambda_T/2$. Therefore, we reconstructed Eq. 9 based on the above findings as follows:

$$q''_{CHF,rough} = K \times \rho_g h_{fg} \left[\frac{\sigma g(\rho_f - \rho_g)}{\rho_g{}^2} \right]^{1/4} + \frac{\pi(\omega_R - \omega_S)\rho_f h_{fg}}{4\lambda_T} \tag{11}$$

Fig. 8(b) shows a comparison of the CHF predicted using Eq. 11 and the experimentally measured CHF. The original Zuber's model has a range of the leading constant K from 0.119 (with λ_D) to 0.157 (with λ_C). To calculate the maximum and minimum CHF lines of Eq. 11, λ_C and λ_D were applied for λ_T, respectively. As a result, the experimentally measured CHFs were located in the prediction range of Eq. 11, as shown in the shaded region of Fig. 8(b). Zuber proposed a value of 0.131 for K; however, compared to our experimental results, this value underestimated K. Thus, it can conclude that the median value of K (0.138) obtained using Zuber's model and the median value of λ_T in Eq. 11, that is $(\lambda_C + \lambda_D)/2$, best fit our experimental results with $R^2 = 0.802$. The URS sample shows a similar tendency to that of sample C, with an error of 6.62% between experimental and predicted values when the mean value of ω_R was used in each direction.

5. Conclusion

In this study, we experimentally investigated and theoretically analyzed the CHF characteristics in pool boiling heat transfer for various rough surfaces using FC-72. In particular, the enhancing effect of the CHF according to the roughness direction was verified in random rough surfaces using the polishing process and in a URS sample obtained from an industrially rolled aluminum plate.

The results of the pool boiling experiments show that the CHF increases with the surface roughness at relatively low roughness but is insignificant in highly rough surfaces. In contrast, the CHF of the URS sample was lower than the highest CHF of random rough surface. The CHF can, therefore, be increased slightly when a surface with directional roughness is polished with a surface roughness of $R_q \sim 0.37$ μm or higher.

The differences in the CHF characteristics for various rough surfaces were verified theoretically based on the surface wetting characteristics. We employed the areal wetting speed as a critical parameter by measuring the wetting distance on rough surfaces to overcome the limitation of CA-based CHF prediction models. As a result, the measured areal wetting speeds with respect to the RMS roughness showed a similar trend to that of experimental CHF result. Finally, a CHF prediction model was proposed to analyze the characteristics of CHF on rough surfaces. The proportional relationship between the increase in CHF and the difference between the areal wetting speed on a rough surface and on a smooth surface was verified. We also verified that the experimental CHF data were located in the median range of the proposed model, which was defined using the range of the Taylor instability wavelength in Zuber's model. In addition, the proposed model can predict the CHF for URS sample using the average of the areal wetting speed in both parallel and normal directions.

Although the proposed CHF prediction model exhibited errors compared to the experimental CHF result, it can predict the trend of enhancement of the CHF on rough surfaces using a simple measurement method. We believe that this method can be widely adopted for estimating the amount of enhancement of the CHF on various surface structures. In the future, we plan to extend this prediction model to engineered surface structures such as micropillar and microchannel.

Declaration of Competing Interest

The authors declare no conflict of interest.

CRediT authorship contribution statement

Jun Kim: Writing - original draft. **Jeongwoo Yeom:** Formal analysis, Visualization. **Daeyoung Kong:** Software, Validation. **Hyoungsoon Lee:** Writing - review & editing. **Seok-min Kim:** Writing - review & editing.

Acknowledgment

This research was supported by the National Research Foundation of Korea (NRF) grant funded by the Korean Government (MSIP) (No. 2015R1A5A1037668).

Supplementary materials

Supplementary material associated with this article can be found, in the online version, at doi:10.1016/j.ijheatmasstransfer.2020.119325.

References

[1] G. Liang, I. Mudawar, Pool boiling critical heat flux (CHF) – Part 1: review of mechanisms, models, and correlations, Int. J. Heat Mass Transf. 117 (2018) 1352–1367, doi:10.1016/j.ijheatmasstransfer.2017.09.134.
[2] N. Lamaison, C.L. Ong, J.B. Marcinichen, J.R. Thome, Two-phase mini-thermosyphon electronics cooling: Dynamic modeling, experimental validation and application to 2U servers, Appl. Therm. Eng. 110 (2017) 481–494, doi:10.1016/j.applthermaleng.2016.08.198.
[3] D.E. Kim, D.I. Yu, D.W. Jerng, M.H. Kim, H.S. Ahn, Review of boiling heat transfer enhancement on micro/nanostructured surfaces, Exp. Therm. Fluid Sci. 66 (2015) 173–196, doi:10.1016/j.expthermflusci.2015.03.023.
[4] V.K. Dhir, Boiling heat transfer, Annu. Rev. Fluid Mech. 30 (1998) 365–401, doi:10.1146/annurev.fluid.30.1.365.
[5] X. Quan, L. Dong, P. Cheng, A CHF model for saturated pool boiling on a heated surface with micro/nano-scale structures, Int. J. Heat Mass Transf. 76 (2014) 452–458, doi:10.1016/j.ijheatmasstransfer.2014.04.037.
[6] M. Mahamudur Rahman, J. Pollack, M. Mccarthy, Increasing boiling heat transfer using low conductivity materials, Sci. Rep. 5 (2015) 12–14, doi:10.1038/srep13145.
[7] J. Wei, J. Zhao, M. Yuan, Y. Xue, Boiling heat transfer enhancement by using micro-pin-finned surface for electronics cooling, Microgravity Sci. Technol. 21 (2009) 159–173, doi:10.1007/s12217-009-9137-5.

[8] S.J. Kim, I.C. Bang, J. Buongiorno, L.W. Hu, Surface wettability change during pool boiling of nanofluids and its effect on critical heat flux, Int. J. Heat Mass Transf. 50 (2007) 4105–4116, doi:10.1016/j.ijheatmasstransfer.2007.02.002.

[9] H.T. Phan, R. Bertossi, N. Caney, P. Marty, S. Colasson, A model to predict the effect of surface wettability on critical heat flux, Int. Commun. Heat Mass Transf. 39 (2012) 1500–1504, doi:10.1016/j.icheatmasstransfer.2012.10.019.

[10] S.G. Kandlikar, A theoretical model to predict pool boiling CHF incorporating effects of contact angle and orientation, J. Heat Transf. 123 (2001) 1071, doi:10.1115/1.1409265.

[11] K.H. Chu, R. Enright, E.N. Wang, Structured surfaces for enhanced pool boiling heat transfer, Appl. Phys. Lett. (2012) 100, doi:10.1063/1.4724190.

[12] T. Nguyen, D. Liu, I. Ka, B. Wang, N. Rashin, Critical heat flux enhancement in pool boiling through increased rewetting on nanopillar array surfaces, Sci. Rep. 8 (2018) 1–9, doi:10.1038/s41598-018-22693-z.

[13] T.L. Liu, C.J.C.J. Kim, Contact angle measurement of small capillary length liquid in super-repelled state, Sci. Rep. 7 (2017) 1–8, doi:10.1038/s41598-017-00607-9.

[14] N.S. Dhillon, J. Buongiorno, K.K. Varanasi, Critical heat flux maxima during boiling crisis on textured surfaces, Nat. Commun. 6 (2015) 1–12, doi:10.1038/ncomms9247.

[15] B.S. Kim, H. Lee, S. Shin, G. Choi, H.H. Cho, Interfacial wicking dynamics and its impact on critical heat flux of boiling heat transfer, Appl. Phys. Lett. (2014) 105, doi:10.1063/1.4901569.

[16] D. Cooke, S.G. Kandlikar, Pool boiling heat transfer and bubble dynamics over plain and enhanced microchannels, J. Heat Transf. 133 (2011) 052902, doi:10.1115/1.4003046.

[17] M.C. Lu, R. Chen, V. Srinivasan, V.P. Carey, A. Majumdar, Critical heat flux of pool boiling on Si nanowire array-coated surfaces, Int. J. Heat Mass Transf. 54 (2011) 5359–5367, doi:10.1016/j.ijheatmasstransfer.2011.08.007.

[18] H.S. Ahn, H.J. Jo, S.H. Kang, M.H. Kim, Effect of liquid spreading due to nano/microstructures on the critical heat flux during pool boiling, Appl. Phys. Lett. 98 (2011) 98–101, doi:10.1063/1.3555430.

[19] H. Lee, T. Maitra, J. Palko, D. Kong, C. Zhang, M.T. Barako, Y. Won, M. Asheghi, K.E. Goodson, Enhanced heat transfer using microporous copper inverse opals, J. Electron. Packag. 140 (2018) 020906, doi:10.1115/1.4040088.

[20] J. Kim, D. Hong, M. Badshah, X. Lu, Y. Kim, S. Kim, Direct metal forming of a microdome structure with a glassy carbon mold for enhanced boiling heat transfer, Micromachines 9 (2018) 376, doi:10.3390/mi9080376.

[21] I. Golobič, K. Ferjančič, Role of enhanced coated surface in pool boiling CHF in FC-72, Heat Mass Transf. Stoffuebertragung 36 (2000) 525–531, doi:10.1007/s002310000118.

[22] K. Ferjančič, I. Golobič, Surface effects on pool boiling CHF, Exp. Therm. Fluid Sci. 25 (2002) 565–571, doi:10.1016/S0894-1777(01)00104-2.

[23] H. Honda, H. Takamatsu, J.J. Wei, Enhanced boiling of FC-72 on silicon chips with micro-pin-fins and submicron-scale roughness, J. Heat Transf. 124 (2002) 383–390, doi:10.1115/1.1447937.

[24] J.J. Wei, H. Honda, Effects of fin geometry on boiling heat transfer from silicon chips with micro-pin-fins immersed in FC-72, Int. J. Heat Mass Transf. 46 (2003) 4059–4070, doi:10.1016/S0017-9310(03)00226-6.

[25] R. Hosseini, a. Gholaminejad, H. Jahandar, Roughness effects on nucleate pool boiling of r-113 on horizontal circular copper surfaces, World Acad. Sci. Eng. Technol. 55 (2011) 679–684.

[26] S.W. Ahmad, T.G. Karayiannis, D.B.R. Kenning, A. Luke, Compound effect of EHD and surface roughness in pool boiling and CHF with R-123, Appl. Therm. Eng. 31 (2011) 1994–2003, doi:10.1016/j.applthermaleng.2011.03.005.

[27] C.K. Guan, B. Bon, J. Klausner, R. Mei, Comparison of CHF enhancement on microstructured surfaces with a predictive model, Heat Transf. Eng. 35 (2014) 452–460, doi:10.1080/01457632.2013.833043.

[28] B.J. Jones, J.P. McHale, S.V. Garimella, The influence of surface roughness on nucleate pool boiling heat transfer, J. Heat Transf. 131 (2009) 121009, doi:10.1115/1.3220144.

[29] J. Kim, S. Jun, R. Laksnarain, S.M. You, Effect of surface roughness on pool boiling heat transfer at a heated surface having moderate wettability, Int. J. Heat Mass Transf. 101 (2016) 992–1002, doi:10.1016/j.ijheatmasstransfer.2016.05.067.

[30] J. Kim, S. Jun, J. Lee, J. Godinez, S.M. You, Effect of surface roughness on pool boiling heat transfer of water on a superhydrophilic aluminum surface, J. Heat Transf. 139 (2017) 101501, doi:10.1115/1.4036599.

[31] C.W. Extrand, S.I. Moon, Contact angles of liquid drops on super hydrophobic surfaces: Understanding the role of flattening of drops by gravity, Langmuir 26 (2010) 17090–17099, doi:10.1021/la102566c.

[32] W. Tong, A. Bar-Cohen, T.W. Simon, S.M. You, Contact angle effects on boiling incipience of highly-wetting liquids, Int. J. Heat Mass Transf. 33 (1990) 91–103, doi:10.1016/0017-9310(90)90144-J.

[33] C.W. Extrand, S. In Moon, When sessile drops are no longer small: transitions from spherical to fully flattened, Langmuir 26 (2010) 11815–11822, doi:10.1021/la1005133.

[34] E. Forrest, E. Williamson, J. Buongiorno, L.W. Hu, M. Rubner, R. Cohen, Augmentation of nucleate boiling heat transfer and critical heat flux using nanoparticle thin-film coatings, Int. J. Heat Mass Transf. 53 (2010) 58–67, doi:10.1016/j.ijheatmasstransfer.2009.10.008.

[35] N.R. Tas, J. Haneveld, H.V. Jansen, M. Elwenspoek, A. Van Den Berg, Capillary filling speed of water in nanochannels, Appl. Phys. Lett. 85 (2004) 3274–3276, doi:10.1063/1.1804602.

[36] J. Bico, C. Tordeux, D. Quere, Rough wetting, Eur. Lett. 55 (2001) 214–220.

[37] S.M. You, T.W. Simon, A. Bar-Cohen, Y.S. Hong, Effects of dissolved gas content on pool boiling of a highly wetting fluid, J. Heat Transf. 117 (2008) 687, doi:10.1115/1.2822631.

[38] S.J. Kline, F.A. McClintock, Describing uncertainties in single-sample experiments, Mech. Eng. 75 (1953) 3–8.

[39] N. Zuber, Hydrodynamic Aspects Of Boiling Heat Transfer (Thesis), 1959, doi:10.2172/4175511.

[40] Y. Haramura, Y. Katto, A new hydrodynamic model of critical heat flux, applicable widely to both pool and forced convection boiling on submerged bodies in saturated liquids, Int. J. Heat Mass Transf. 26 (1983) 389–399, doi:10.1016/0017-9310(83)90043-1.

[41] A.K. Rajvanshi, J.S. Saini, R. Prakash, Investigation of macrolayer thickness in nucleate pool boiling at high heat flux, Int. J. Heat Mass Transf. 35 (1992) 343–350, doi:10.1016/0017-9310(92)90272-T.

[42] Y. Hayata, Distribution of void fraction above a horizontal heating surface in pool boiling, Bull. JSME. 12 (1969) 283–290.

[43] Y. Katto, S. Yokoya, Principal mechanism of boiling crisis in pool boiling, Int. J. Heat Mass Transf. 11 (1968) 993–1002.

[44] A.M. Bhat, J.S. Saini, R. Prakash, Role of macrolayer evaporation in pool boiling at high heat flux, Int. J. Heat Mass Transf. 29 (1986) 1953–1961, doi:10.1016/0017-9310(86)90014-1.